Enhanced long-lived dark photon signals at lifetime frontier detectors

Mingxuan Du,[1] Rundong Fang,[1] Zuowei Liu,[1,2] and Van Que Tran[1,3,*]

[1]*Department of Physics, Nanjing University, Nanjing 210093, China*
[2]*CAS Center for Excellence in Particle Physics, Beijing 100049, China*
[3]*Faculty of Fundamental Sciences, PHENIKAA University, Yen Nghia, Ha Dong, Hanoi 12116, Vietnam*

(Received 18 December 2021; accepted 23 February 2022; published 14 March 2022)

Long-lived particles that are present in many new physics models beyond the standard model, can be searched for in a number of newly proposed lifetime frontier experiments at the LHC. The signals of the long-lived dark photons can be significantly enhanced in a new dark photon model in which dark photons are copiously produced in the hidden radiation process. We investigate the capability of various lifetime frontier detectors in probing the parameter space of this model, including the far forward detectors FACET and FASER, the far transverse detector MATHUSLA, and the precision timing detector CMS-MTD. We find that the accessible parameter space is significantly enlarged by the hidden radiation process so that FACET, MATHUSLA, and CMS-MTD can probe a much larger parameter space than the so-called minimal model. The parameter space probed by FACET is found to be much larger than FASER, which is largely due to the fact that the former has a larger decay volume and is closer to the interaction point. There also exists some parameter space that can be probed both by the far detectors and by precision timing detectors, so that different experiments can be complementary to each other. A brief overview of the lifetime frontier detectors is also given.

DOI: 10.1103/PhysRevD.105.055012

I. INTRODUCTION

Particles with a macroscopic decay length, ranging from a few centimeters to several hundred meters and beyond, can be classified as long-lived particles (LLPs) at the large hadron collider (LHC). Such LLPs are endemic in new physics models beyond the standard model (SM); see, e.g., [1,2] for recent reviews. A number of new detectors at the LHC have been recently proposed to search for LLPs, which can be collectively referred to as lifetime frontier detectors. These include the detectors that are placed in the forward region: FACET [3,4], FASER [5–9], FASER2 [9,10], AL3X [11], and MoEDAL-MAPP [12]; the detectors that are placed in the central region: MATHUSLA [13–17], CODEX-b [18,19], ANUBIS [20]; and the precision timing detectors that are to be installed at ATLAS, CMS, and LHCb to mitigate the pileup backgrounds in the coming HL-LHC phase: CMS-MTD [21], ATLAS-HGTD [22], LHCb-TORCH [23,24]. A plethora of LLPs can be studied in the newly proposed lifetime frontier detectors [25–59].

One well-motivated new physics particle is the dark photon (denoted by A'_μ) which can naturally arise in kinetic mixing model [60,61], in Stueckelberg models [62–66] [45]. The interaction between the dark photon A'_μ and the SM fermion f can be parametrized as

$$e\epsilon Q_f A'_\mu \bar{f}\gamma^\mu f. \tag{1}$$

Long-lived dark photons (LLDPs) have a small ϵ coupling, which, however, leads to a suppressed collider signal. Recently, a new dark photon model is proposed in Ref. [45] where the dark photon is produced at colliders by the hidden fermion radiation so that the collider signal no longer suffers from the small ϵ parameter. For that reason, the LLDP signal at the LHC in this new dark photon model can be significantly enhanced.[1] Thus, we will refer to the dark photon models, where the dark photon interacts with the SM sector only via the interaction Lagrangian in Eq. (1), as the "minimal" dark photon models, to be distinguished from the dark photon models proposed in Ref. [45].

In this paper, we investigate the capability of various lifetime frontier detectors in probing the parameter space of LLDPs both in the minimal dark photon model and in the newly proposed dark photon model [45]. We carry out

*Present address: Tsung-Dao Lee Institute, Shanghai Jiao Tong University, 520 Shengrong Road, Shanghai 200240, China.

Published by the American Physical Society under the terms of the Creative Commons Attribution 4.0 International license. Further distribution of this work must maintain attribution to the author(s) and the published article's title, journal citation, and DOI. Funded by SCOAP³.

[1]See [39,43,67,68] for other dark photon models with a sizeable LLDP signal.

detailed analysis for detectors: the far forward detector, FACET and FASER, the central transverse detector, MATHUSLA, and the precision timing detector, CMS-MTD. We compute the expected limits from these detectors. We find that the parameter space probed by FACET and MATHUSLA are significantly enlarged by the hidden fermion radiation in the new dark photon model, as compared to the minimal dark photon model. We also find that the LLDP signal at the newly proposed far detector FACET is significantly larger than FASER, owing to a larger decay volume and a shorter distance to the interaction point of the FACET detector.

The rest of the paper is organized as follows. We briefly review the dark photon model that has an enhanced LLDP signal in Sec. II. A mini-overview on lifetime-frontier detectors is given in Sec. III. We discuss three main DP production channels in Sec. IV. We analyze the signal events in different lifetime-frontier detectors in Sec. V. Given in Sec. VI are the sensitivities to the parameter space from four different detectors: FACET, FASER (2), MATHUSLA, and CMS-MTD. A semianalytic comparison between far detectors is given in Sec. VII. We summarize our findings in Sec. VIII.

II. THE MODEL AND ITS PARAMETER SPACE

In this analysis, we consider the dark photon model that has been proposed recently to enhance the (suppressed) long-lived dark photon signal at the LHC [45]. In this model, the standard model is extended by a hidden sector that consists of two Abelian gauge groups $U(1)_F$ and $U(1)_W$ with corresponding gauge bosons X_μ and C_μ, respectively, and one Dirac fermion ψ charged under both gauge groups [45]. The gauge boson mass terms (due to the Stueckelberg mechanism [62–66]) and the gauge interaction terms in the hidden sector are given by

$$\begin{aligned}\mathcal{L} = &-\frac{1}{2}(\partial_\mu\sigma_1 + m_1\epsilon_1 B_\mu + m_1 X_\mu)^2 \\ &-\frac{1}{2}(\partial_\mu\sigma_2 + m_2\epsilon_2 B_\mu + m_2 C_\mu)^2 \\ &+ g_F\bar{\psi}\gamma^\mu\psi X_\mu + g_W\bar{\psi}\gamma^\mu\psi C_\mu, \end{aligned} \tag{2}$$

where B_μ is the hypercharge boson in the SM, σ_1 and σ_2 are the axion fields in the Stueckelberg mechanism, g_F and g_W are the gauge coupling constants, and m_1, m_2, $m_1\epsilon_1$, and $m_2\epsilon_2$ are mass terms in the Stueckelberg mechanism with $\epsilon_{1,2}$ being (small) dimensionless numbers.

The 2 by 2 neutral gauge boson mass matrix in the SM is extended to a 4 by 4 mass matrix due to the fact that the two new gauge bosons, X_μ and C_μ, have mixed mass terms with the SM hypercharge boson B_μ; the new neutral gauge boson mass matrix in the basis of $V = (C, X, B, A^3)$ is given by [45]

$$M^2 = \begin{pmatrix} m_2^2 & 0 & m_2^2\epsilon_2 & 0 \\ 0 & m_1^2 & m_1^2\epsilon_1 & 0 \\ m_2^2\epsilon_2 & m_1^2\epsilon_1 & \sum_{i=1}^2 m_i^2\epsilon_i^2 + \frac{g'^2v^2}{4} & -\frac{g'gv^2}{4} \\ 0 & 0 & -\frac{g'gv^2}{4} & \frac{g^2v^2}{4} \end{pmatrix} \tag{3}$$

where A^3 is the third component of the $SU(2)_L$ gauge bosons, g and g' are gauge couplings for the SM $SU(2)_L$ and $U(1)_Y$ gauge groups respectively, and $v = 246$ GeV is the vacuum expectation value of the SM Higgs boson.

Diagonalization of the mass matrix (via an orthogonal transformation $\mathcal{O}$) leads to the mass eigenstates $E = (Z', A', Z, A)$ with $E_i = \mathcal{O}_{ji}V_j$ where A is the SM photon, Z is the SM Z boson, A' is the dark photon, and Z' is the new heavy boson. The interaction Lagrangian between the mass eigenstates of the neutral gauge bosons and the fermions is given by [45]

$$[\bar{f}\gamma_\mu(v_i^f - \gamma_5 a_i^f)f + v_i^\psi\bar{\psi}\gamma_\mu\psi]E_i^\mu \tag{4}$$

where f is the SM fermion. The small coupling v_4^ψ between the hidden fermion ψ and the SM photon can be rewritten as $v_4^\psi \equiv e\delta$ where δ is usually referred to as "millicharge".

Figure 1 shows various experimental constraints on the model, including the constraints from millicharged particle searches [69–71], the electroweak precision measurements for the Z mass shift [45], the Z invisible decay [72], the dilepton high mass resonance search at ATLAS [73], and the monojet search at ATLAS [74]. Here we choose $m_1 = 3$ GeV, $m_2 = 700$ GeV, $g_F = 1.5$, $g_W = 1$, and $\epsilon_1 \ll \epsilon_2$.

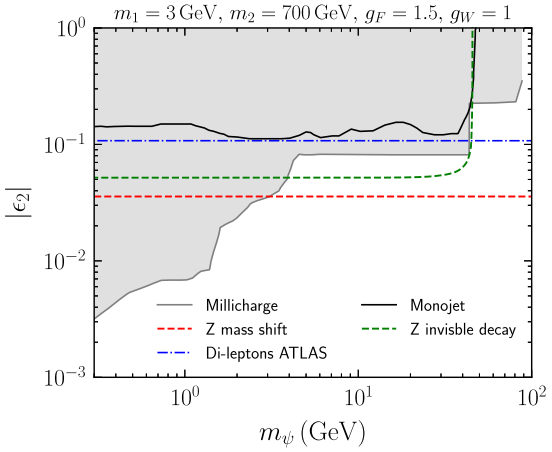

FIG. 1. The upper bound on ϵ_2 as a function of m_ψ. The other parameters are $m_1 = 3$ GeV, $m_2 = 700$ GeV, $g_F = 1.5$, $g_W = 1.0$, and $\epsilon_1 \ll \epsilon_2$. Here $\epsilon_2 \simeq (-g'/g_W)\delta$ where δ is the millicharge of ψ. The limits include the constraints on millicharged particles (shaded light gray) [69–71], the electroweak precision measurements for the Z mass shift (dashed red) [45], the Z invisible decay (dashed green) [72], the dilepton high mass resonance search at ATLAS (dash-dotted blue) [73], and the monojet search at ATLAS (solid black) [74].

Throughout this analysis we use $m_2 = 700$ GeV, $g_F = 1.5$, and $g_W = 1$ as the default values for these three parameters as in Ref. [45]; in the parameter space of interest, we have $m_1 \simeq \text{GeV} \ll m_2$ so that the dark photon mass $m_{A'} \simeq m_1$, and the heavy Z' boson has a mass $m_{Z'} \simeq m_2$. For the hidden fermion mass $m_\psi \gtrsim 3$ GeV the electroweak constraint on the Z mass shift gives the most stringent limit, $\epsilon_2 \lesssim 0.036$, whereas for the mass range 0.3 GeV $\lesssim m_\psi \lesssim$ 3 GeV, the leading constraints come from the recent ArgoNeuT data [70] and the milliQan demonstrator data [71]. We note that the mass fraction of the millicharged DM is constrained to be $\lesssim$0.4% by the CMB data [75–77], which is satisfied in the parameter space of interest of our model [45].

III. A MINI-OVERVIEW ON LIFETIME-FRONTIER DETECTORS

A number of new lifetime-frontier detectors have been proposed recently at the LHC, which can be used to search for LLPs. Table I shows the angular coverage, location, size, and expected running time of these new detectors. We classify the detectors into three categories: forward detectors, central transverse detectors, and precision timing detectors. The forward detectors include FACET [3,4], FASER [5–9], FASER2 [9,10], AL3X [11], and MoEDAL-MAPP [12]. The central transverse detectors include CODEX-b [18,19], MATHUSLA [13–17], ANUBIS [20]. The precision timing detectors include CMS-MTD [21], ATLAS-HGTD [22], and LHCb-TORCH [23,24]. Below we provide a mini-overview of the new lifetime frontier detectors.

A. Forward detectors

FASER (the ForwArd Search ExpeRiment), is located at 480 m downstream of the ATLAS detector along the beam axis [5–9]. FASER has a cylindrical decay volume of length $L = 1.5$ m and radius $R = 10$ cm. FASER has been installed at the TI12 tunnel at the LHC and is expected to collect data during LHC Run 3 (2022) [79]. The upgrade version, FASER 2, with a decay volume of length $L = 5$ m and radius $R = 1$ m is proposed to be installed during the HL-LHC run (2026-35) [9,10].

FACET (Forward-Aperture CMS ExTension) is a new lifetime frontier detector which is proposed to be installed ~100 m upstream of the CMS detector along the beam axis [3,4]. FACET is proposed to be built based on the CMS Phase 2 Upgrade concept, combining silicon tracker, timing detector, HGCAL-type EM/HAD calorimeter, and GEM-type muon system in a compact design [3,4,80]; the latest design of the FACET detector is shown in Fig. 2. The decay volume of the FACET experiment is an enlarged LHC quality vacuum beam pipe which is 18 m long and has a radius of 50 cm [3,4,80,81]. The FACET detector is shielded by about 35-50 m of steel (in the Q1-Q3 quadrupoles and D1 dipole) in front of it [81]; additional shielding materials are placed before the decay volume, as shown in Fig. 2. The FACET detector, surrounding the LHC beam pipe which has a radius $R = 18$ cm, is placed behind the decay volume. As a new proposed far forward detector, FACET has some merits. The 35-50 m steel shielding before FACET, corresponding to 200–300 nuclear interaction lengths, is comparable to the shielding material for FASER, which is ~100 m of concrete/rock, corresponding

TABLE I. Proposed detectors for long-lived particles searches at the LHC. The first column shows the detector name, the second column shows the pseudorapidity coverage, the third column shows the distance from interaction point (IP) to the near side of the detector and the location (to the far side of the detector, for FASER), the fourth column shows the decay volume of the detector, and the last column shows the starting time of data-taking. The first five detectors are located at the forward region of the corresponding IP; the middle three detectors are located at the far central transverse region of the corresponding IP; the last three detectors are the precision timing detectors to be installed at CMS, ATLAS and LHCb respectively to control the HL-LHC pile-up background. The HL-LHC is expected to start data-taking in 2027 (run 4) [78]. Here "upstream" ("downstream") means that the detector is located in the clockwise (anticlockwise) direction of the corresponding IP, viewed from above.

Detector	η	Distance from IP (m)	Decay volume (m^3)	LHC runs
FACET [3,4]	[6, 7.2]	100 (upstream)	12.3	Run 4 (2027)
FASER [5–9]	>9	480 (downstream)	0.047	Run 3 (2022)
FASER2 [9,10]	>6.87	480 (downstream)	15.7	HL-LHC
AL3X [11]	[0.9, 3.7]	5.25 (upstream)	915.2	Run 5 (2032)
MoEDAL-MAPP [12]	~3.1	55 (upstream)	~150	Run 3 (2022)
CODEX-b [18,19]	[0.14, 0.55]	26 (transverse)	10^3	Run 4 (2027)
MATHUSLA [13–17]	[0.64, 1.43]	60 (transverse)	2.5×10^5	HL-LHC
ANUBIS [20]	[0.06, 0.21]	24 (transverse)	$\sim 1.3 \times 10^4$	HL-LHC
CMS-MTD [21]	$[-3, 3]$	1.17 (barrel), 3.04 (endcaps)	25.4	HL-LHC
ATLAS-HGTD [22]	[2.4, 4]	3.5 (endcaps)	8.7	HL-LHC
LHCb-TORCH [23,24]	[1.6, 4.9]	9.5 (beam direction)	⋯	HL-LHC

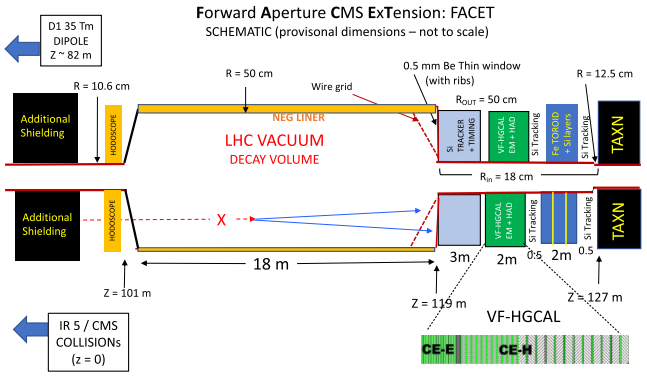

FIG. 2. Schematic layout of the proposed FACET detector (side view) [82].

to ∼240 nuclear interaction lengths. FACET will benefit from the high quality LHC vacuum pipe as the decay volume [3,4,80]. FACET plans to have both the EM and HAD calorimeters [81], whereas FASER has only EM calorimeter [6–9]. This allows FACET to have a better detection efficiency for the hadronic decays of the DP, especially for the neutral hadronic decays.

AL3X (A Laboratory for Long-Lived eXotics) is an on-axis cylindrical detector which has been proposed to be installed at ALICE experiment during the LHC Run 5 [11]. The detector will make use of the existing ALICE time projection chamber and the L3 electromagnet. It is also envisioned to move the ALICE detector by 11.25 m downstream from its current location, providing space for a spherical shell segment of tungsten to shield the detector from the IP. The AL3X detector is then expected to be located 5.25 m away from the IP along the beam axis, with a 12 m long cylindrical decay volume of a 0.85 m inner radius and a 5 m outer radius.

The MoEDAL-MAPP detector is the MAPP (Apparatus for the detection of Penetrating Particles) detector at MoEDAL (Monopole and Exotics Detector at the LHC) [12], which is proposed to be installed at the UGCI gallery near the LHCb experiment (IP8) in future LHC runs. MoEDAL-MAPP is 55 m from IP8 and with an angle of 5° away from the beam line, with a fiducial volume of ∼150 m^3 [12].

B. Central detectors

CODEX-b (Compact Detector for Exotics at LHCb) has been proposed to be constructed at the LHCb cavern [18,19]. The decay volume is designed to be 10 m × 10 m × 10 m. It is located ∼5 m in the z axis (beam direction) and ∼26 m in the transverse direction away from the LHCb IP, with a pseudorapidity coverage of $0.14 < \eta < 0.55$. The demonstrator detector, CODEX-β (about 2 m × 2 m × 2 m) has been developed for the LHC Run 3 [19].

MATHUSLA (MAssive Timing Hodoscope for Ultra-Stable neutraL pArticles) is a new proposed experiment near the ATLAS or CMS IP [13–17]. It is proposed to be placed ∼68 m downstream from the IP and ∼60 m above the LHC beam axis with a decay volume of 100 m × 100 m × 25 m [17]. MATHUSLA was previously proposed to be installed at ∼100 m downstream from the IP and ∼100 m above the LHC beam axis with a decay volume of 200 m × 200 m × 20 m [13–16]. In this analysis, we adopt the parameters from the recent proposal [17].

ANUBIS (AN Underground Belayed In-Shaft search experiment) [20] is a new proposed experiment taking advantage of the 18 m diameter, 56 m long PX14 installation shaft of the ATLAS experiment. The proposed detector consists of four tracking stations which have the same cross section area of 230 m^2 and are 18.5 m apart from each other.

C. Precision timing detectors

To mitigate the high pile-up background at the HL-LHC, various precision timing detectors will be installed at CMS [21], ATLAS [22,83,84], and LHCb [23], which can be used for LLP searches [30,32,40,45,49,55,85,86].[2]

The CMS-MTD detector consists of the precision minimum ionizing particle (MIP) timing detector with a timing resolution of 30 picoseconds [21]. The timing layers will be installed between the inner trackers and the electromagnetic calorimeter for the barrel and endcap regions. The timing detector in the barrel region has a length of 6.08 m along the beam axis direction and a transverse distance of 1.17 m away from the beam. The timing detectors in the endcap regions have a pseudorapidity coverage of $1.6 < |\eta| < 3.0$ and are located ∼3.0 m from the IP. The decay volume of LLPs at CMS-MTD is ∼25.4 m^3 if one demands that the LLPs decay before arriving at the timing layers and the decay vertex has a transverse distance of 0.2 m $< L_T <$ 1.17 m from the beam axis [30,49].

The HGTD (High Granularity Timing Detector) has been proposed to be installed in front of the ATLAS endcap and forward calorimeters at $z = \pm 3.5$ m from the IP during the ATLAS Phase-II upgrade [22,83,84]. The ATLAS-HGTD can cover the pseudorapidity range of $2.4 < |\eta| < 4.0$, and is expected to have a time resolution of 35 ps (70 ps) per hit at the start (end) of HL-LHC [84]. The decay volume of ATLAS-HGTD is ∼8.7 m^3, if LLPs are required to decay before arriving at the timing detector and the decay vertex has a transverse distance of 0.12 m $< L_T <$ 0.64 m [84].

The TORCH (Time Of internally Reflected CHerenkov light) detector has been proposed to be installed at the next upgrade of LHCb [23]. The TORCH will be located at $z \sim 9.5$ m from the LHCb IP with the angular acceptance of

[2]For early studies on precise timing, see, e.g., Ref. [87], where the precise timing method was proposed to search for LLPs or stable particles in a beam dump experiment. Such a search was later carried out in the E733 experiment at Fermilab [88].

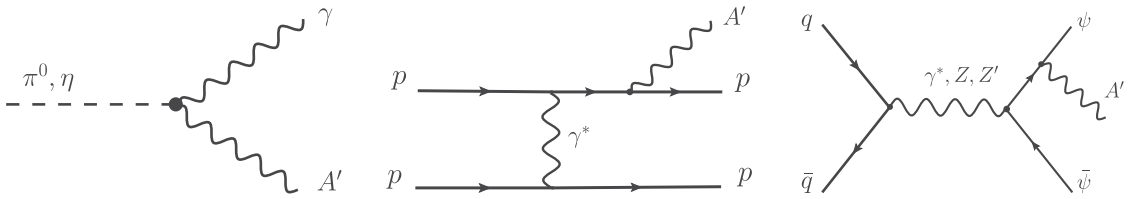

FIG. 3. Feynman diagrams for the dark photon production at the LHC: from meson decays (left), from the proton bremsstrahlung (middle), and from the hidden fermion radiation (right).

$1.6 < \eta < 4.9$. The precision of each track in the TORCH system is 15 ps [23].

IV. THE DARK PHOTON PRODUCTION

In our model, there are three main processes to produce dark photon A' at the LHC: rare meson decays (hereafter MD), coherent proton bremsstrahlung (hereafter PB), and hidden sector radiation (hereafter HR); the corresponding Feynman diagrams are shown in Fig. 3. The MD and PB processes are common for the dark photon models, because dark photons are produced via interactions between the dark photon and charged particles in the SM in these two processes. The HR process is new in our model [45], which is mediated by the interaction between the dark photon and the hidden sector particle ψ.[3]

A. Meson decays

Dark photons can be produced in the $m \to \gamma + A'$ process, where m denotes a light meson, as shown in the left diagram in Fig. 3; the branching ratio can be computed via [89]

$$\mathrm{BR}(m \to A' + \gamma) = 2\epsilon^2 \left(1 - \frac{M_{A'}^2}{M_m^2}\right)^3 \mathrm{BR}(m \to \gamma\gamma), \tag{5}$$

where ϵ is the coupling constant given in Eq. (1). In the parameter space of interest of our model, one has $\epsilon \approx (0.27/e)\epsilon_1$ for $m_1 \lesssim 30$ GeV. For light mesons, one has $\mathrm{BR}(\pi^0 \to \gamma\gamma) \simeq 0.99$ and $\mathrm{BR}(\eta \to \gamma\gamma) \simeq 0.39$ [90]. Since light mesons can be copiously produced in the forward direction at high energy pp collisions, (for example, the production cross section of π^0 (η) in each hemisphere at the LHC is 1.6×10^{12} pb (1.7×10^{11} pb) [7]), dark photon from rare meson decays can be a leading dark photon production mode at the LHC if the decay is kinematically allowed [5]. We neglect the $m \to A'A'$ process because we have $\epsilon \ll 1$ for the LLDP.

[3]Here we do not consider the dark photon direct production channel which consists of the following processes $q\bar{q} \to A'$, $q\bar{q} \to gA'$, $qg \to qA'$, and $\bar{q}g \to \bar{q}A'$, because they suffer from large PDF uncertainties for sub-GeV A' and are suppressed by ϵ_1 which is much smaller than ϵ_2 in the HR process.

In our analysis, we generate the four-momentum spectrum for the π^0/η mesons using the EPOS-LHC [91] model in CRMC [92] with 10^5 simulation events of pp inelastic collision at the LHC with $\sqrt{s} = 13$ TeV. We then boost the momentum of the dark photon (which is isotropically distributed in the π^0/η rest frame) to the lab frame, by using the meson momentum. Our simulations are found to be consistent with FORESEE [10]. We also simulate the heavy mesons D^0, B^0, and J/ψ using PYTHIA 8 [93]. We found that the DP production cross section due to decays of these heavy mesons is about five orders of magnitude smaller than the light mesons (π^0 and η). Therefore we neglect the contribution from heavy meson decays in our analysis.

B. Proton bremsstrahlung

Proton bremsstrahlung process is another major production mode of light dark photons in high energy pp collisions; the Feynman diagram is shown as the middle diagram in Fig. 3. The dark photon signal arising from the proton bremsstrahlung process can be computed by the Fermi-Weizsacker-Williams (FWW) method [94–96], in which the proton is treated as a coherent object; the total number of the dark photon produced in a far forward detector[4] is given by [5]

$$N_{A'}^{\mathrm{PB}} = \mathcal{L}|F_1(m_{A'}^2)|^2 \int dz\, dp_T^2 \sigma_{pp}(s') w(z, p_T^2) \times \Theta(\Lambda_{\mathrm{QCD}}^2 - q_{\mathrm{min}}^2), \tag{6}$$

where $N_{A'}^{\mathrm{PB}}$ is the number of dark photon events from the PB process, $\mathcal{L}$ is the integrated luminosity, F_1 is the form factor function, $z = p_{A'}^L/p_p$ with $p_{A'}^L$ being the longitudinal momentum of the dark photon and p_p the proton beam momentum, p_T is the transverse momentum of the dark photon, $\sigma_{pp}(s')$ is the inelastic cross section [97] with $s' = 2m_p(E_p - E_{A'})$ in the rest frame of one of the colliding protons, $w(z, p_T^2)$ is the splitting function, $\Lambda_{\mathrm{QCD}} \simeq 0.25$ GeV is the QCD scale, and q is the momentum carried by the virtual photon in the middle diagram in Fig. 3. The splitting function $w(z, p_T^2)$ in Eq. (6) is given by [98–100]

[4]For a near detector with nearly 4π coverage, e.g., CMS, one can use the FWW method to compute the PB contributions from each colliding proton in the lab frame.

$$w(z,p_T^2) \simeq \frac{\epsilon^2\alpha}{2\pi H}\left\{\frac{1+(1-z)^2}{z} - 2z(1-z)\left(\frac{2m_p^2+m_{A'}^2}{H} - z^2\frac{2m_p^4}{H^2}\right)\right. \tag{7}$$

$$\left. + 2z(1-z)(z+(1-z)^2)\frac{m_p^2 m_{A'}^2}{H^2} + 2z(1-z)^2\frac{m_{A'}^4}{H^2}\right\}, \tag{8}$$

where $H = p_T^2 + (1-z)m_{A'}^2 + z^2 m_p^2$. To guarantee the validity of the FWW approximation, the Heaviside function Θ is imposed in Eq. (6) with the minimal virtuality of the photon cloud around the beam proton given by [99,100]

$$|q_{\min}^2| \approx \frac{1}{4E_p^2 z^2(1-z)^2}[p_T^2 + (1-z)m_{A'}^2 + z^2 m_p^2]^2. \tag{9}$$

The form factor $F_1(p_{A'}^2)$ in Eq. (6) is given by [5,101]

$$F_1(p_{A'}^2) = \sum_{V=\rho\rho'\rho''\omega\omega'\omega''} \frac{f_V m_V^2}{m_V^2 - {p'_A}^2 - i m_V \Gamma_V}, \tag{10}$$

where m_V (Γ_V) is the mass (decay width) of the vector meson, $f_\rho = 0.616$, $f_{\rho'} = 0.223$, $f_{\rho''} = -0.339$, $f_\omega = 1.011$, $f_{\omega'} = -0.881$, and $f_{\omega''} = 0.369$.

C. Hidden radiation

Dark photons can also be produced via hidden fermion radiations in the HR process, as shown in the third diagram of Fig. 3. Within certain parameter space of the models in Ref. [45], the HR process can be more important than the MD and PB processes. For the models considered in this analysis, dark photons in the HR process are produced at the LHC in the radiation process of the hidden sector fermion ψ, which are pair-produced at the LHC via the $q\bar{q} \to \gamma^*/Z/Z' \to \bar{\psi}\psi$ process, as shown in the third diagram in Fig. 3.

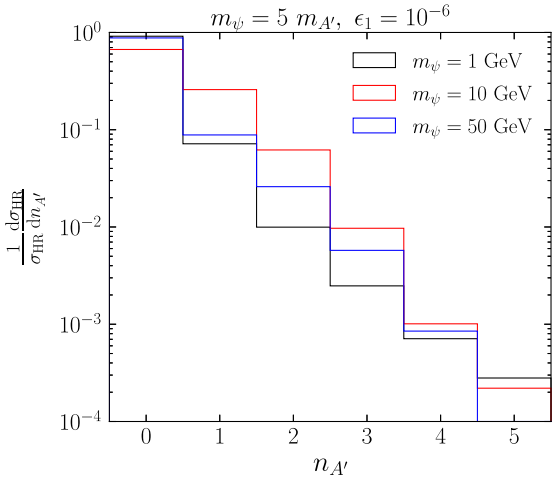

FIG. 4. The normalized distribution of dark photon multiplicity in the $\psi\bar{\psi}$ events, where $\sigma_{\rm HR}$ is the $\psi\bar{\psi}$ cross section. We take $m_\psi = 5m_{A'}$ and $\epsilon_1 = 10^{-6}$. The black, red, and blue histograms are for the $m_\psi = 1$ GeV, 10 GeV, and 50 GeV cases respectively.

In the MD and PB processes, the dark photon production cross section is suppressed by the small ϵ parameter [given in Eq. (1)] needed for the long lifetime of the dark photon. In the HR process, however, the LHC production of ψ is not controlled by ϵ so that the LHC cross section of ψ can be sizable even for heavy ψ.

To obtain the contribution from the HR process, we use FeynRules [102] to produce the UFO file for our model, which is then passed into MADGRAPH 5 [103] to generate the $pp \to \psi\bar{\psi}$ events at the LHC. We further use PYTHIA 8 [93,104,105] to simulate the dark radiation process of the ψ particle to obtain the dark photons.

The dark photon cross section in the HR process at the LHC can be computed via

$$\sigma_{A'}^{\rm HR} = \bar{n}_{A'}\sigma(pp \to \psi\bar{\psi}), \tag{11}$$

where $\bar{n}_{A'}$ is the expected number of dark photons per $\psi\bar{\psi}$ event, and $\sigma(pp \to \psi\bar{\psi})$ is the production cross section of the $\psi\bar{\psi}$ events at the LHC. We compute $\bar{n}_{A'}$ by taking the ratio of the total number of dark photons in our PYTHIA simulation to the number of $\psi\bar{\psi}$ events simulated. We note that multiple dark photons can be radiated by one ψ fermion; see e.g., Refs. [67,106–108] for some earlier studies on dark vector bosons radiated from hidden sector fermions. Figure 4 shows the normalized distribution of the number of dark photons in the $\psi\bar{\psi}$ events for three benchmark models in our simulation with the relation $m_\psi = 5m_{A'}$; the expected dark photon number are $\bar{n}_{A'} \simeq 0.097$, 0.42 and 0.16 for $m_\psi = 1$, 10 and 50 GeV cases respectively.

We compare three different contributions to $\sigma(pp \to \psi\bar{\psi})$ at the LHC from three different mediators (photon, Z, and Z') in Fig. 5, where the interference effects have been neglected.[5] We use MADGRAPH 5[103] to compute the cross sections, where we have fixed $m_{A'} = 0.4$ GeV, $\epsilon_1 = 6 \times 10^{-7}$, and $\epsilon_2 = 0.005$. For $m_\psi \lesssim 8$ GeV the dominant contribution to the $\psi\bar{\psi}$ pair-production cross section comes from the s-channel photon process; for

[5]We neglect the process mediated by the dark photon since it is suppressed by the small ϵ parameter needed for LLDP so that it is several orders of magnitude smaller than the other three mediators in our analysis.

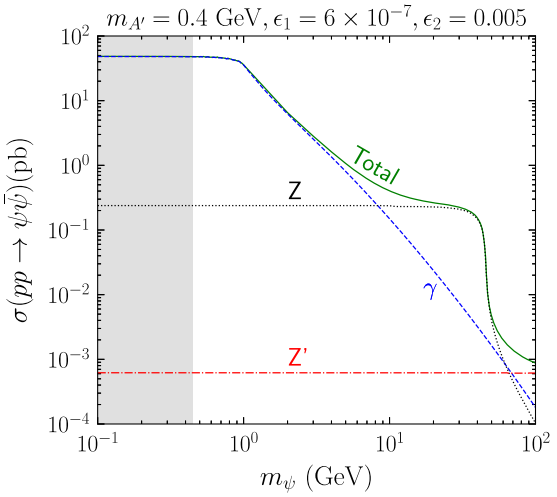

FIG. 5. The contributions to the $pp \to \psi\bar{\psi}$ cross section at the LHC from three different mediators: γ (blue-dashed), Z (black-dotted), Z' (red-dashdotted). The total cross section (green-solid) taking into account all contributions (including the A' contribution and the interference terms) is also shown. We use $\epsilon_1 = 6 \times 10^{-7}$, $\epsilon_2 = 0.005$, and $m_{A'} = 0.4$ GeV. The gray shaded region indicates the parameter space excluded by the millicharge constraints [69–71]. We use NNPDF23LO [109] which is the default PDF in MADGRAPH 5.

higher ψ mass, the contributions from Z and Z' exchanges become more important.

D. Comparison of the three DP production channels

In Fig. 6, we compare the three dark photon production channels (MD, PB, and HR) at the LHC, both in the 4π solid angle and in the very forward region. The very forward region is defined by the dark photon pseudorapidity $\eta_{A'} > 6$.[6] We choose $\epsilon_1 = 10^{-6}$ and $\epsilon_2 = 0.005$ for both figures in Fig. 6.

The left panel figure of Fig. 6 shows the dark photon cross sections as a function of the hidden fermion mass m_ψ for the case where the dark photon mass is fixed at $m_{A'} \simeq 0.4$ GeV. The dark photon cross section in the HR process decreases with the hidden fermion mass m_ψ; the cross sections in the MD and PB processes are independent of m_ψ, since these processes do not involve the hidden fermion ψ. For light ψ the HR process dominates the MD and PB processes, whereas for heavy ψ the MD and PB processes become more important. In particular, the HR process dominates the dark photon production if $m_\psi \lesssim 5$ GeV (30 GeV) in the very forward (4π solid angle) region.

The right panel figure of Fig. 6 shows the dark photon cross sections as a function of the dark photon mass $m_{A'}$ for the case where $m_\psi = 5m_{A'}$. The HR process dominates the entire mass range except the small resonance region near $m_{A'} \simeq 0.8$ GeV, where the PB process becomes larger. We note that, in the right panel of Fig. 6, the resonance in the PB process is due to the pole structure (due to various vector mesons) in the form factor given in Eq. (10), and the kink features in the MD cross section arise because of the mass threshold effects in meson decays.

About 10% of the dark photons in the MD and PB processes are produced in the very forward region as shown in Fig. 6. For the HR process, the number of dark photons produced in the very forward region is sizable in the low ψ mass region, with a fraction up to ~15% for $m_\psi \simeq 0.5$ GeV, as shown in the left panel figure of Fig. 6. For heavy ψ mass the cross section in the very forward region is significantly reduced, for example, less than 1% of the dark photon in the HR process produced in the forward region when $m_\psi \gtrsim 6$ GeV. This is because heavier ψ particles tend to be produced more isotropically than lighter ψ particles and thus lead to fewer events in the forward region.

E. PDF uncertainties

For light ψ one has to integrate over the small x region in PDFs where there are large uncertainties [5]. In the process $pp \to \psi\bar{\psi}$, the minimum value of x is $x_{\min} = 4m_\psi^2/s$, if there is no cut on the ψ momentum. Thus, for the $m_\psi = 15(0.5)$ GeV case, one has to integrate over the x range near $x_{\min} \simeq 5 \times 10^{-6}(6 \times 10^{-9})$. The minimum value of x is 10^{-9} in the PDFs sets: NNPDF23LO [109], NNPDF40 [110], and CT18 [111]. Thus, for the $m_\psi = 0.5$ GeV case, the dark photon production cross section in the HR process (denoted as $\sigma_{A'}^{\rm HR}$) depends on the PDFs in the x region where PDFs begin. To check the stability of the LHC cross sections (of small m_ψ) against different PDFs, we compute various LHC cross sections including $\sigma(pp \to \psi\bar{\psi})$, $\sigma_{A'}^{\rm HR}$ in the 4π angular region, $\sigma_{A'}^{\rm HR}$ in the forward region $\eta_{A'} > 6$, and $\sigma_{A'}^{\rm HR}$ in the FACET detector, by using three different PDFs: NNPDF23LO (the default PDFs in MADGRAPH 5), NNPDF40, and CT18, in Fig. 7.

For $\sigma(pp \to \psi\bar{\psi})$ at $m_\psi \simeq 0.5$ GeV, the NNPDF40 (CT18) leads to a cross section that is about 30% (45%) of that from NNPDF23; for $\sigma_{A'}^{\rm HR}$ in the 4π angular region, these two percentage numbers become 55% (80%). This is because the ψ particles have to be energetic enough to radiate dark photons, which then corresponds to larger $x_{\min}$ values in the PDF integration, leading to less PDF uncertainties. The PDF uncertainties in the 4π angular region are smaller than the forward region, which is due to the fact that the 4π region includes the region with significant transverse momentum.

In the sensitivity contours of FACET as shown in Fig. 10, the mass of ψ has to satisfy $m_\psi \gtrsim 1.5$ GeV to be consistent with the millicharge constraints. We find that NNPDF40 (CT18) leads to a cross section of ~33% (~64%) of

[6]The angular acceptance of FACET is $6 < \eta < 7.2$ [3,4], and the angular acceptance of FASER is $\eta > 9$ [6–9].

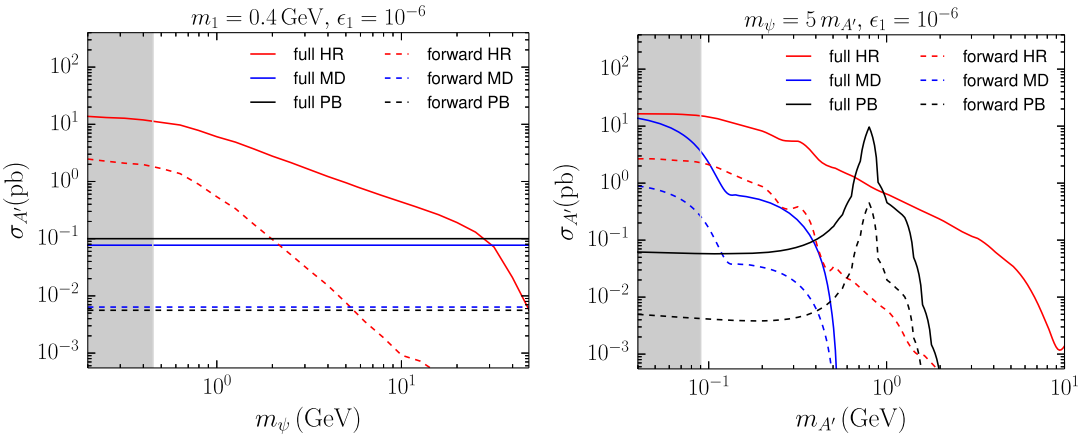

FIG. 6. The LHC production cross section of dark photon $\sigma_{A'}$ from three contributions: HR (red lines), MD (blue lines) and PB (black lines). The solid lines correspond to the cross section in full solid angle, and the dashed lines represent the cross section in the very forward region with $\eta_{A'} > 6$. Here we use $\epsilon_1 = 10^{-6}$ and $\epsilon_2 = 0.005$ for both panels; we choose $m_1 = 0.4$ GeV in the left panel and $m_1 = 0.2 m_\psi$ in the right panel. The gray shaded region ($m_\psi \lesssim 0.45$ GeV for $\epsilon_2 = 0.005$) indicates the parameter space excluded by the millicharge constraints [69–71].

NNPDF23 at $m_\psi \simeq 1.5$ GeV, as shown in Fig. 7. For the $m_\psi \simeq 15$ GeV case (the ψ mass in Fig. 9), we find that the cross section computed with NNPDF40 (CT18) is ∼80% (∼97%) of that with NNPDF23, in Fig. 7. Thus the PDF uncertainty on our sensitivity contours is less significant. Furthermore, the sensitivity contours analyzed with different PDFs, as shown in Fig. 10, show that different PDFs only modify the limits for small ϵ_1 values (the lower edge of the contours), but have unnoticeable effects on large ϵ_1 values (the upper edge of the contours). This is due to the fact that the large ϵ_1 values correspond to small decay lengths, and thus the dark photon should have a significant momentum to decay inside the far detectors. For that reason, the $x_{\min}$ in the PDF integration becomes larger for the model points with large ϵ_1 values, resulting in insignificant PDF uncertainty.

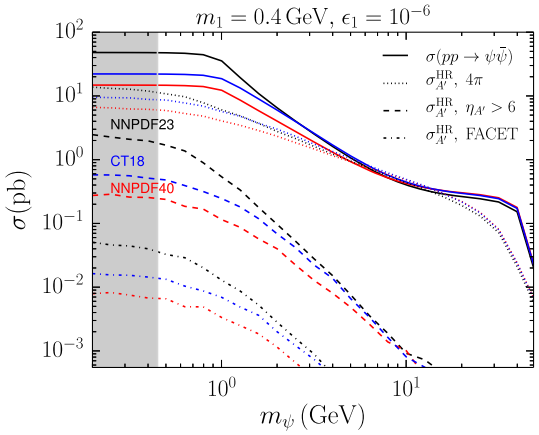

FIG. 7. Comparison of LHC cross sections using different PDFs. The LHC cross sections of $\sigma(pp \to \psi\bar{\psi})$ (solid), $\sigma(A')$ of the HR process in the 4π angular region (dotted), in the forward region $\eta_{A'} > 6$ (dashed), and in the FACET detector (dashdotted) are computed with NNPDF23 [109] (black), NNPDF40 [110] (red), and CT18 [111] (blue).

V. ANALYSIS

In this analysis, we investigate the LLDP signals in the following four detectors: FACET, FASER, MATHUSLA, and CMS-MTD. We carry out analysis for the model points in the parameter space spanned by the DP mass $m_{A'}$ and the DP lifetime $\tau_{A'}$. For each model point, we compute the DP signal events from the MD, PB and HR processes. For the MD and PB processes, we obtain the DP momentum and the position of its decay vertex, by using the simulations discussed in Sec. IV A and Sec. IV B, respectively. We then boost the daughter particles from dark photon decays to the lab frame, from the rest frame of the dark photon, where the daughter particles are isotropic. For the HR process, we use MADGRAPH 5 [103] to generate 10^6 events for the $pp \to \psi\bar{\psi}$ process, and use PYTHIA 8 [93,104,105] to simulate the hidden radiation of the ψ particle and the decay of the dark photon, which outputs the momentum information for the DP and its daughter particles, as well as the decay position of the DP. To expedite the analysis (only a small fraction of simulated events from PYTHIA 8 are actually inside the decay volume of the detectors), we disregard the decay position of the dark photon provided by PYTHIA 8 and use the dark photons that decay both inside and outside of the decay volume.

Thus, for the three far detectors (FACET, FASER, MATHUSLA), we compute the probability of detecting a DP as follows

$$P_{A'} = f(\theta, \phi) \int_{L_{\min}}^{L_{\max}} d\ell \frac{e^{-\ell/\ell_{A'}}}{\ell_{A'}} \omega, \tag{12}$$

where $L_{\rm min}$ ($L_{\rm max}$) is the minimal (maximum) distance between the decay volume and the IP along the (θ,ϕ) direction with θ and ϕ the polar and azimuthal angles of the dark photon respectively, $\ell_{A'}=\tau_{A'}|\vec{p}_{A'}|/m_{A'}$ is the decay length of dark photon with $\tau_{A'}$ being the lifetime, $f(\theta,\phi)$ describes the angular acceptance of the decay volume, and ω equals 1 if the decay final states of the DP satisfy additional detector cuts (ω equals 0 otherwise).

For a cylindrical detector (e.g., FASER and FACET) that is placed along the beam direction with a distance d from the IP to the near side of the detector, the parameters in Eq. (12) are given by

$$L_{\rm min}=d,\qquad L_{\rm max}=d+L, \tag{13}$$

$$f(\theta,\phi)=\Theta(R/L_{\rm min}-\tan\theta)\Theta(\tan\theta-r/L_{\rm max}), \tag{14}$$

where L is the length of decay volume of the detector, r (R) is the inner (outer) radius of the decay volume, and Θ is the Heaviside step function. For the FACET detector, one has $r=18$ cm and $R=50$ cm; for the FASER (FASER 2) detector, one has $r=0$ and $R=10$ (100) cm. For the cylindrical forward detectors, the pseudorapidity range is often used to describe the acceptance of the detectors, $f(\theta,\phi)=\Theta(\eta_{\rm max}-\eta_{A'})\Theta(\eta_{A'}-\eta_{\rm min})$. Thus for the FACET detector, one has $\eta_{\rm min}\simeq 6$ and $\eta_{\rm max}\simeq 7.2$[7]; for the FASER (FASER 2) detector, one has $\eta_{\rm min}\simeq 9$ (7) and $\eta_{\rm max}=+\infty$.

For a box-shape detector with height H, width W, length L and is located at a distance d from the IP along the z-axis and a distance h above the LHC beam (along the x-axis) (e.g., MATHUSLA), one has[8]

$$L_{\rm max}=\begin{cases}\frac{h+H}{\sin\theta\cos\phi} & \text{if } \tan\theta>\frac{h+H}{(d+L)\cos\phi}\ \&\ |\tan\phi|<\frac{W}{2(h+H)},\\ \frac{d+L}{\cos\theta} & \text{if } \tan\theta<\frac{h+H}{(d+L)\cos\phi}\ \&\ |\sin\phi|<\frac{W}{2(d+L)\tan\theta},\\ \frac{W}{2\sin\theta|\sin\phi|} & \text{if } |\sin\phi|>\frac{W}{2(d+L)\tan\theta},\end{cases} \tag{15}$$

$$L_{\rm min}=\begin{cases}\frac{h}{\sin\theta\cos\phi} & \text{if } \tan\theta<\frac{h}{d\cos\phi},\\ \frac{d}{\cos\theta} & \text{if } \tan\theta>\frac{h}{d\cos\phi},\end{cases} \tag{16}$$

$$f(\theta,\phi)=\Theta\left(\tan\theta-\frac{h}{(d+L)\cos\phi}\right)\Theta\left(\frac{h+H}{d\cos\phi}-\tan\theta\right)\Theta\left(\frac{W}{2h}-|\tan\phi|\right)\Theta(\cos\phi). \tag{17}$$

For the MATHUSLA detector, we use $d=68$ m, $h=60$ m, $W=100$ m, $L=100$ m, and $H=25$ m [17].

For FACET, we further require both daughter particles from the DP decay to traverse both the tracker and the calorimeter detectors. For the FASER detector, we further apply a detector cut on the energy of DP daughter particles $E_{\rm vis}>100$ GeV [7] to reduce the trigger rate and remove possible background (BG) at low energies. For the FACET detector, because the BG events are expected to be highly suppressed due to the front shielding and the high quality vacuum of the decay volume, no detector cut is required. For the MATHUSLA detector, we require both DP daughter particles to hit the ceiling detector and are well separated with an opening angle $\Delta\theta>0.01$ [14]; we note that $\omega=0$ for the second and third lines of Eq. (15), by requiring such a cut.

Thus the number of events in the far detector can be obtained

$$N=\mathcal{L}\cdot\sigma_{A'}\cdot\langle P_{A'}\rangle\quad\text{with}\quad\langle P_{A'}\rangle=\frac{1}{N_{A'}}\sum_{i=1}^{N_{A'}}P_{A'_i}, \tag{18}$$

where $\sigma_{A'}$ is the total DP production cross section, $\langle P_{A'}\rangle$ denotes the average detection probability of the DP event, $N_{A'}$ is the total number of the DP in the simulation and $P_{A'_i}$ is the individual detection probability of the ith dark photon event in the simulation which is given by Eq. (12).

For the CMS-MTD detector, we only consider the DPs produced from the HR process for the CMS-MTD analysis. This is because the CMS-MTD detector does not have sensitivity to the DP mass below ~GeV [45]. Following Ref. [45], we use MADGRAPH 5 to generate $\psi\bar{\psi}$ events with an ISR jet to time stamp the event, i.e., $pp\to\psi\bar{\psi}j$ where the ISR jet is required to have $p_T>30$ GeV and $|\eta|<2.5$. The DP is required to have a transverse decay length $0.2\text{ m}<\ell^T_{A'}<1.17$ m and a longitudinal decay length $|z_{A'}|<3.04$ m. The final state leptons from DP decays

[7] $\eta_{\rm min}\simeq 6$ corresponds to the left-upper corner of the decay volume, and $\eta_{\rm max}\simeq 7.2$ corresponds to the right-bottom (inner radius) corner of the upper half of the decay volume as shown in Fig. 2.

[8] Note the distance d here is different from that in Table I.

are detected by the precision timing detector; the leading lepton should have $p_T > 3$ GeV. The time delay variable [30] between the ISR jet and the leading lepton is required to $\Delta t > 1.2$ ns [45].

VI. RESULT

In this section we discuss the projected sensitivities of the future LLP detectors including FACET, FASER, MATHUSLA and the precision timing detector CMS-MTD. Our main results are shown in Figs. 8, 9, 10, 11, where sensitivity contours for far detectors are made by requiring the new physics events to be $N = 5$, under the assumption that the SM processes do not contribute any event in the decay volume after various shieldings and detector cuts. We are only interested in the parameter space in which $m_{A'} < 2m_\psi$ so that the dark photon is kinematically forbidden to decay into

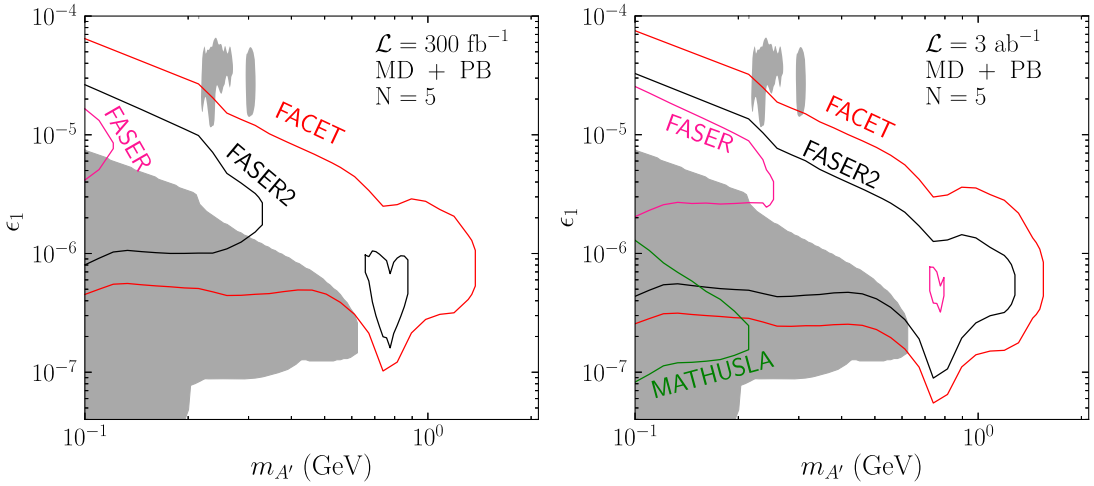

FIG. 8. Projected sensitivities from FACET (red), FASER (magenta), FASER2 (black), and MATHUSLA (green), at the HL-LHC with the integrated luminosities of $\mathcal{L} = 300$ fb^{-1} (left panel) and $\mathcal{L} = 3$ ab^{-1} (right panel) to the "minimal" dark photon models in which only the MD and PB processes contribute to the signals. Contours correspond to the expected signal events $N = 5$. The dark gray shaded region indicates the parameter space that has been excluded by various experiments including LHCb [112], ν-CAL I [113,114], CHARM [115], and E137 [116]; the limits are obtained with the Darkcast package [117].

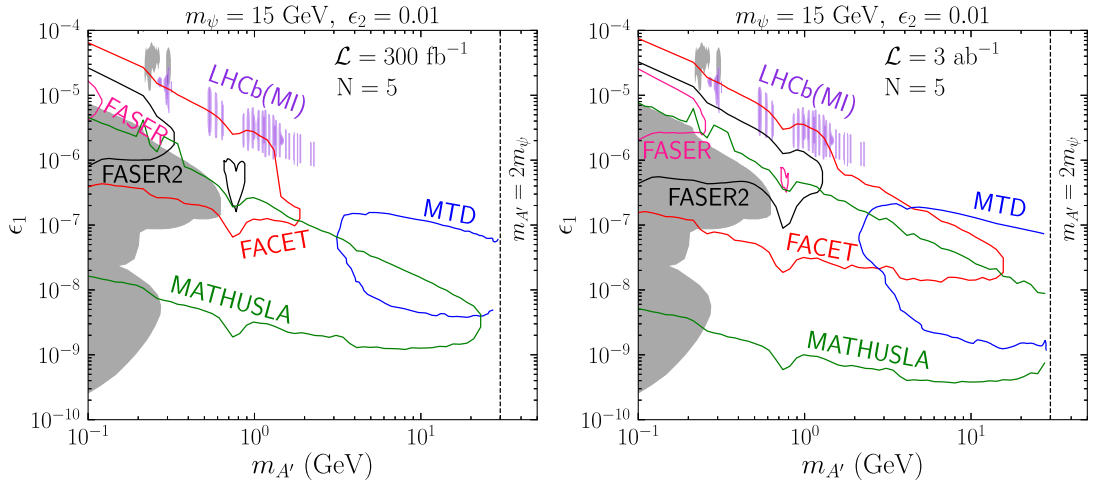

FIG. 9. Projected sensitivities from FACET (red), FASER (magenta), FASER2 (black), and MATHUSLA (green), at the HL-LHC with the integrated luminosities of $\mathcal{L} = 300$ fb^{-1} (left panel) and $\mathcal{L} = 3$ ab^{-1} (right panel) to our dark photon model in which all the three dark photon production channels (MD, PB, and HR) contribute to the signals. Here we fix $m_\psi = 15$ GeV and $\epsilon_2 = 0.01$, and require $m_{A'} < 2m_\psi$ so that the dark photon cannot decay into invisible final states. Contours correspond to the expected signal events $N = 5$. The dark gray shaded region indicates the excluded dark photon parameter space by various experiments including LHCb [112], ν-CAL I [113,114], CHARM [115], E137 [116], LSND [118], and SN1987A [119] where the HR process is not considered; the limits are obtained with the Darkcast package [117]. The purple shaded regions are excluded by recasting the model-independent (MI) constraints from the displaced dimuon search at the LHCb [120] on the HR process.

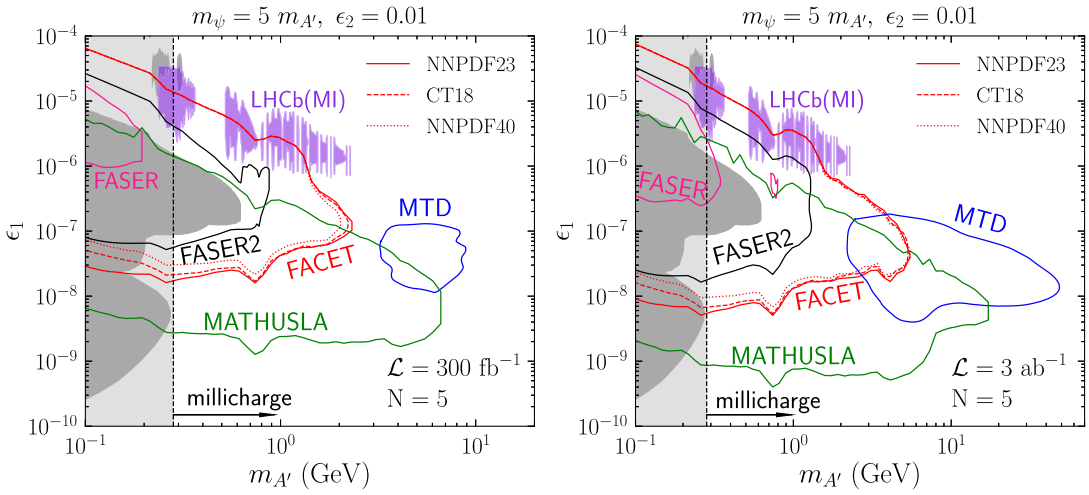

FIG. 10. Same as Fig. 9 except $m_\psi = 5m_{A'}$. The light gray region is excluded by the millicharge constraints [69–71]. For the FACET contours we use NNPDF23 [109] (red-solid), CT18 [111] (red-dashed), and NNPDF40 [110] (red-dotted).

the hidden fermion pair, leading to a long-lived dark photon.[9]

Figure 8 shows the projected sensitivities on the minimal dark photon models with 300 fb^{-1} and 3 ab^{-1} data, from FACET, FASER, FASER2, and MATHUSLA. We also exhibit various experimental constraints including LHCb [112], ν-CAL I [113,114], CHARM [115], and E137 [116]. We only include the MD and PB processes here; the HR process is absent. For that reason, the analysis in Fig. 8 is also applicable to the minimal dark photon model. Among the new detectors, the parameter space probed by FACET is larger than the other experiments. In particular, with an integrated luminosity of 300 fb^{-1} (3 ab^{-1}) at the HL-LHC, FACET can probe the DP mass up to ∼1.3 GeV (1.5 GeV), whereas FASER can only probe the DP mass up to ∼0.12 GeV (0.25 GeV plus the island near 0.79 GeV), and FASER2 can only probe the DP mass up to ∼0.8 GeV (1.3 GeV). Because DPs arising from the PB and MD processes are likely to be distributed in the forward region, MATHUSLA, a detector located in the central transverse region, has difficulties to probe the parameter space of the minimal dark photon model. For that reason, MATHUSLA only probe a small parameter region with 3 ab^{-1} data, which, however, has been excluded already by the current experimental constraints. We note that the dips at $m_{A'} \sim 0.8$ GeV in the contours are due to the resonance in the PB process, and the kink features at $m_{A'} \sim 0.2$ GeV are due to the mass threshold effects in the MD process.

Figure 9 shows the projected sensitivities for our dark photon models from FACET, FASER, FASER2, MATHUSLA, and CMS-MTD. Here the dark photon production contributions from all channels including the MD, PB and HR processes are considered. With the inclusion of the HR process, the FACET and MATHUSLA sensitivity contours are significantly enlarged to heavier DP mass region, as compared to Fig. 8; the FASER and FASER2 sensitivity contours, on the other hand, are similar to those in Fig. 8. With 300 fb^{-1} (3 ab^{-1}) data at the HL-LHC, FACET can probe the parameter space of our model up to $m_{A'} \simeq 1.9(15)$ GeV. The CMS-MTD probes a relative large dark photon mass region: down to dark photon mass ∼3(2) GeV for 300 fb^{-1} (3 ab^{-1}) data at HL-LHC. This is due to the fact that a light dark photon leads to not only a small time delay but also small transverse momenta of the final state leptons, which will suffer from a large SM background for the time delay searches [45]. Interestingly, this CMS-MTD sensitivity region partly overlaps with MATHUSLA sensitivity region for the luminosity of 300 fb^{-1}, and with both FACET and MATHUSLA sensitivity regions for the luminosity of 3 ab^{-1}. Thus, if a dark photon in this overlap region is discovered, one can see the FACET and MATHUSLA to verify the results from the CMS-MTD.

Figure 10 shows the expected limits from FACET, FASER, FASER2, MATHUSLA, and CMS-MTD to the parameter space of our dark photon model with the mass relation $m_\psi = 5m_{A'}$. The sensitivity contours are similar to Fig. 9, but with some changes. For light ψ, the millicharge constraints are important, which excludes the parameter space $m_{A'} \lesssim 0.3$ GeV (corresponding to $m_\psi > 1.5$ GeV for $\epsilon_2 = 0.01$). The parameter space probed by FASER with $\mathcal{L} = 300$ fb^{-1} (3 ab^{-1}) at the HL-LHC is (nearly) excluded by the millicharge constraints. Further, the heavy dark photon mass region can no longer be probed by various detectors as in Fig. 9. This is because the heavy dark photon mass corresponds to the heavy ψ mass via the mass relation $m_\psi = 5m_{A'}$, which then leads to a suppressed $pp \to Z^* \to \psi\psi$ cross section. Similar to the result in Fig. 9, the

[9]If $m_{A'} > 2m_\psi$, the dark photon can decay into a pair of hidden fermions, which then leads to a prompt decay dark photon, assuming an order-one gauge coupling in the hidden sector.

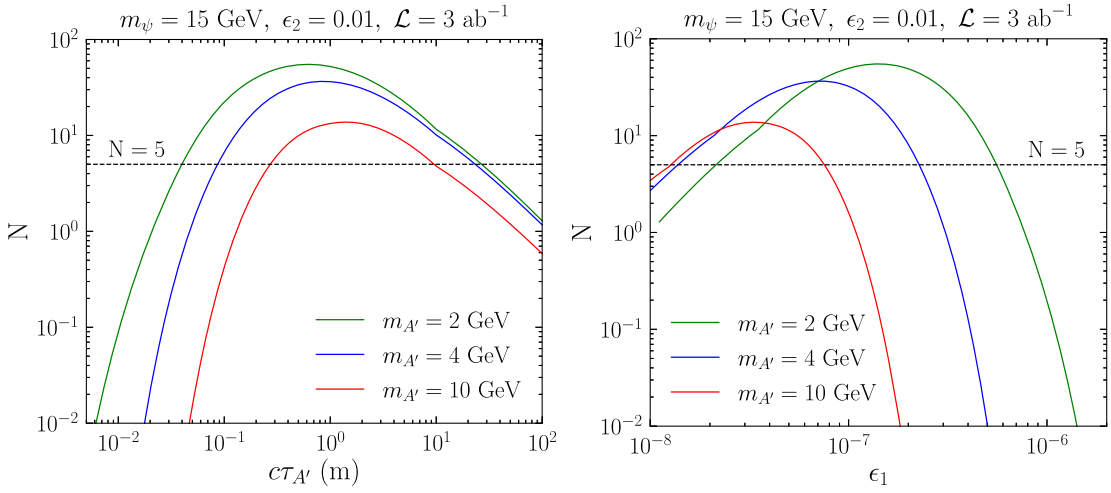

FIG. 11. The number of signal events in the FACET detector at the HL-LHC with $\mathcal{L} = 3$ ab^{-1}, as a function of the DP lifetime $c\tau_{A'}$ (left panel) and of the coupling ϵ_1 (right panel). Here we fix $m_\psi = 15$ GeV and $\epsilon_2 = 0.01$, and vary the dark photon mass to be $m_{A'} = 2$ GeV (green), 4 GeV (blue), and 10 GeV (red).

CMS-MTD sensitivity region is partly overlapped with FACET and MATHUSLA. To check the PDF uncertainties on the sensitivity contours, we further compute the FACET contours using three different sets of PDFs: NNPDF23 [109] (red-solid), CT18 [111] (red-dashed), and NNPDF40 [110] (red-dotted). As shown in Fig. 10, the upper edge of the FACET contours from the three PDFs are almost identical; the lower edge of the FACET contours from the three PDFs, however, can be seen with some visible differences from each other. For example, for $m_{A'} \sim 0.3$ GeV, the lower edge of the FACET contours with 300 fb^{-1} are located at $\epsilon_1 = 1.9 \times 10^{-8}$ with NNPDF23, $\epsilon_1 = 2.3 \times 10^{-8}$ with CT18, and $\epsilon_1 = 3.2 \times 10^{-8}$ with NNPDF40, as shown on the left panel figure of Fig. 10; for 3ab^{-1} data, ϵ_1 are 5.9×10^{-9}, 7.3×10^{-9}, and 1.0×10^{-8} respectively, as shown on the right panel figure of Fig. 10. Thus different PDFs will result in changes to the FACET contours but the effects are not significant.

Model-independent constraints on LLPs with a displaced vertex of several centimeters in the dimuon channel have been recently analyzed by LHCb [120], which used the same data sample (5.1 fb^{-1}) as the analysis optimized for the minimal dark photon model [112], but with a different fiducial region and selection cuts. The 90% CL upper bounds on the LLP cross section $\sigma(X \to \mu^+\mu^-)$ are provided for various LLP masses in the range $0.214\ \text{GeV} < m_X < 3$ GeV and for three p_T^X bins: 2–3 GeV, 3–5 GeV, and 5–10 GeV [120]. This allows us to recast the limits to the HR process in our model.[10] Following Ref. [120], we select events with muon transverse momentum $p_T(\mu) > 0.5$ GeV, muon momentum $10 < p(\mu) < 1000$ GeV, muon pseudorapidity $2 < \eta(\mu) < 4.5$, and $p_T(\mu^+)p_T(\mu^-) > 1$ GeV^2. We further require that the DP has a transverse momentum of $2 < p_T(A') < 10$ GeV, a pseudorapidity of $2 < \eta(A') < 4.5$, and a transverse decay length of $12 < \ell_{A'}^T < 30$ mm, and the opening angle of the dimuon pair is larger than 3 mrad. We then rule out a model point in the parameter space if it produces a cross section exceeding the upper bound in any of the three p_T bins. We show the excluded parameter space by this model-independent LHCb analysis (purple shaded regions) in Figs. 9 and 10. For the minimal dark photon, the excluded regions are the two gray "islands" at ~0.2–0.3 GeV [112]. For our dark photon model, the excluded regions by the LHCb model-independent limits are much larger, extending beyond ~2 GeV in the dark photon mass and down to $\epsilon_1 \sim 10^{-6}$, which already rule out some parameter space to be probed by FACET and FASER2 detectors.

The left panel in Fig. 11 shows the number of signal events in the FACET detector as a function of the proper lifetime, for three different dark photon masses. The number of events decreases with the dark photon mass. The peak of the distribution of the events shifts to a larger $c\tau_{A'}$ value when the dark photon mass increases. The peak shift is due to the detector cut on the DP decay length: a larger $c\tau_{A'}$ is needed for a heavier DP mass so that the DP has the desired decay length to disintegrate in the FACET decay volume. With the criterion of $N > 5$ events, FACET can probe the $c\tau_{A'}$ range of [0.04 m–30 m] for DP mass $m_{A'} = 2$ GeV, $c\tau_{A'} \in [0.09\ \text{m–}25\ \text{m}]$ for $m_{A'} = 4$ GeV, and $c\tau_{A'} \in [0.3\ \text{m} - 10\ \text{m}]$ for $m_{A'} = 10$ GeV. The right panel in Fig. 11 shows the number of signal events in the FACET detector as a function of the parameter ϵ_1. With the criterion of $N > 5$ events, FACET can probe the

[10]The MD and PB processes in our model is the same as the minimal DP model. According to Ref. [120], the new LHCb analysis [120] is only half sensitive in probing the minimal DP model, as compared with the previous LHCb analysis [112]. Thus, we exclude the MD and PB processes in our simulation and only consider the HR process.

$\epsilon_1 \in [2.1 \times 10^{-8}$–$5.5 \times 10^{-7}]$ for DP mass $m_{A'} = 2$ GeV, $\epsilon_1 \in [1.4 \times 10^{-8}$–$2.3 \times 10^{-7}]$ for $m_{A'} = 4$ GeV, and $\epsilon_1 \in [1.3 \times 10^{-8}$–$7.5 \times 10^{-8}]$ for $m_{A'} = 10$ GeV.

VII. EXPECTED NUMBER OF EVENTS IN FAR DETECTORS

Here we provide an approximated expression for the number of dark photon events in the far detectors, and also compare the number of events for two far detectors that are of different sizes and placed with different distances from the IP.

Denote the cross sectional area of the decay volume of a far detector as A and the length as L; the volume of the decay volume is then $V = AL$. If the far detector is placed at a distance d from the IP with $d \gg L$, the probability of the DP to decay within the interval $(d, d + L)$ can be approximated by

$$P \simeq \exp\left[-\frac{d}{\ell_{A'}}\right]\frac{L}{\ell_{A'}}, \tag{19}$$

where $\ell_{A'}$ is the decay length of the DP. The number of DPs that disintegrate inside the decay volume is then given by

$$N \simeq N_{\rm IP}\frac{A}{4\pi d^2}P = N_{\rm IP}\frac{1}{4\pi}\frac{V}{d^3}\exp\left[-\frac{d}{\ell_{A'}}\right]\frac{d}{\ell_{A'}}, \tag{20}$$

where $N_{\rm IP}$ is the total number of DPs produced at the IP, and we have assumed an isotropic distribution for DPs for simplicity. Thus for given N_i, V, and d, the optimal decay length to be probed is $\ell_{A'} = d$. Equation (20) also suggests that in order to obtain a large signal of LLPs, one should build a large decay volume and place it close to the IP if the SM backgrounds are under control; see also [121] for a similar discussion.

Next we compare two detectors with different V and d. The ratio of the number of events is given by

$$\frac{N_1}{N_2} = \frac{V_1}{V_2}\left[\frac{d_2}{d_1}\right]^2\exp\left[-\frac{d_1 - d_2}{\ell_{A'}}\right]. \tag{21}$$

Using the parameters given in Table I, we find that $N_{\rm FACET}/N_{\rm FASER} \simeq 7 \times 10^3 \exp(380\ {\rm m}/\ell_{A'})$. Thus the number of events in FACET is at least 7×10^3 times larger than FASER, if one neglects the background considerations and other effects. This is the main reason that the contours of FACET sensitivity are much larger than FASER. Similarly, we find that $N_{\rm FACET}/N_{\rm FASER2} \simeq 18 \exp(380\ {\rm m}/\ell_{A'})$. We find that these ratios between FACET and FASER(2) estimated here are consistent with the results from our simulations.[11]

[11]For example, for the model point $m_{A'} = 0.5$ GeV and $\epsilon_1 = 2.9 \times 10^{-7}$ in Fig. 10, we find that $N_{\rm FACET}/N_{\rm FASER} \simeq 8400$ and $N_{\rm FACET}/N_{\rm FASER2} \simeq 33$ in our simulations.

VIII. SUMMARY

We study the capability of the various new lifetime frontier experiments in probing long-lived dark photon models. We consider both the minimal dark photon model, and the dark photon model proposed by some of us recently that has an enhanced long-lived dark photon signal at the LHC.

In the new dark photon model that has an enhanced long-lived dark photon signal at the LHC, the standard model is extended by the Stueckelberg mechanism to include a hidden sector, which consists of two gauge bosons and one Dirac fermion ψ. The Stueckelberg mass terms eventually lead to a GeV-scale dark photon A' and a TeV-scale Z' with couplings ϵ_1 and ϵ_2 to the SM sector respectively. The dark photon signal at the LHC in this new model is enhanced because it is proportional to ϵ_2 which can be significantly larger than ϵ_1, which is small so that the dark photon is long-lived. We compute various experimental constraints on the ϵ_2 parameter including the most recent constraints on millicharge from the ArgoNeuT and milliQan demonstrator experiments. We also take into account the experimental constraints on the ϵ_1 parameter, including our recasting of the recent LHCb model-independent limits on the HR process in our model.

There are three major production channels for the long-lived dark photon in the parameter space of interest: the MD, PB, and HR processes. The MD and PB are present in both the minimal dark photon model and the new dark photon model, and are mostly distributed in the forward region. The HR process, however, is only present in the new dark photon model, and has significant contributions to both the forward region and the transverse region (but still with dominant contributions in the forward region). We find that the HR process provides the dominant contributions for large dark photon mass, which opens up new parameter space to be probed by various new lifetime-frontier detectors.

We provide a mini-overview on the various lifetime-frontier detectors and select four detectors for further detailed analysis, which include the far detectors FACET, FASER (and its upgraded version, FASER2), and MATHUSLA, and the future precision timing detector CMS-MTD. We compute the sensitivity contours in the parameter space spanned by the dark photon mass and the parameter ϵ_1. For example, with 300 fb^{-1} (3 ab^{-1}) data at the HL-LHC, FACET can probe the parameter space up to $m_{A'} \simeq 1.9(15)$ GeV, for the case where $m_\psi = 15$ GeV. We find that the sensitivity contours from FACET and MATHUSLA are significantly enlarged by the HR process, and the CMS-MTD is only sensitive to the HR process. The enhancement in the central transverse detector MATHUSLA is mainly due to the fact that the MD and PB events are highly concentrated in the forward direction, and the HR process has some significant contributions in the transverse direction.

We further compare the signal events between the two far forward detectors: FACET and FASER. We find that FACET is likely to detect many more events than FASER, which is mainly due to the larger decay volume of the FACET detector and its smaller distance from the interaction point. The FASER2 detector, with a much larger decay volume than FASER, can somewhat offset the effects of the long distance from the interaction point. Thus we find that the FACET contours are larger than FASER and FASER2 in our analysis.

We also find that there exists parameter space that can be probed by different kinds of lifetime-frontier experiments. Thus, for example, if a long-lived dark photon signal were found in one precision timing detector (e.g., CMS-MTD), it could then be verified by a far forward detector (e.g., FACET) and a far transverse detector (e.g., MATHUSLA).

ACKNOWLEDGMENTS

We thank Michael Albrow for correspondence and discussions on FACET and for some suggestions on the FACET analysis. We thank Greg Landsberg for correspondence and comments on the millicharge constraints and on the dark photon model. We thank Michael William for correspondence on the recent LHCb model-independent analysis. The work is supported in part by the National Natural Science Foundation of China under Grant No. 11775109.

[1] L. Lee, C. Ohm, A. Soffer, and T.-T. Yu, Collider searches for long-lived particles beyond the standard model, Prog. Part. Nucl. Phys. **106**, 210 (2019).
[2] J. Alimena *et al.*, Searching for long-lived particles beyond the standard model at the large hadron collider, J. Phys. G **47**, 090501 (2020).
[3] G. Landsberg, Searches for new physics with FACET: Forward-apertrue CMS extension, https://indico.cern.ch/event/994582/.
[4] S. Cerci *et al.*, FACET: A new long-lived particle detector in the very forward region of the CMS experiment, arXiv:2201.00019.
[5] J. L. Feng, I. Galon, F. Kling, and S. Trojanowski, Forward search experiment at the LHC, Phys. Rev. D **97**, 035001 (2018).
[6] FASER Collaboration, Letter of intent for FASER: Forward search experiment at the LHC, arXiv:1811.10243.
[7] FASER Collaboration, FASER's physics reach for long-lived particles, Phys. Rev. D **99**, 095011 (2019).
[8] FASER Collaboration, Technical proposal for FASER: Forward search experiment at the LHC, arXiv:1812.09139.
[9] FASER Collaboration, FASER: Forward search experiment at the LHC, arXiv:1901.04468.
[10] F. Kling and S. Trojanowski, Forward experiment sensitivity estimator for the LHC and future hadron colliders, Phys. Rev. D **104**, 035012 (2021).
[11] V. V. Gligorov, S. Knapen, B. Nachman, M. Papucci, and D. J. Robinson, Leveraging the ALICE/L3 cavern for long-lived particle searches, Phys. Rev. D **99**, 015023 (2019).
[12] MoEDAL Collaboration, Meeting of the Division of Particles and Fields of the American Physical Society, arXiv:1910.05772.
[13] J. P. Chou, D. Curtin, and H. J. Lubatti, New detectors to explore the lifetime frontier, Phys. Lett. B **767**, 29 (2017).
[14] D. Curtin *et al.*, Long-lived particles at the energy frontier: The MATHUSLA physics case, Rep. Prog. Phys. **82**, 116201 (2019).
[15] MATHUSLA Collaboration, A letter of intent for MATHUSLA: A dedicated displaced vertex detector above ATLAS or CMS, arXiv:1811.00927.
[16] M. Nessi, Explore the lifetime frontier with MATHUSLA, J. Instrum. **15**, C06026 (2020).
[17] MATHUSLA Collaboration, An update to the letter of intent for MATHUSLA: Search for long-lived particles at the HL-LHC, arXiv:2009.01693.
[18] V. V. Gligorov, S. Knapen, M. Papucci, and D. J. Robinson, Searching for long-lived particles: A compact detector for exotics at LHCb, Phys. Rev. D **97**, 015023 (2018).
[19] G. Aielli *et al.*, Expression of interest for the CODEX-b detector, Eur. Phys. J. C **80**, 1177 (2020).
[20] M. Bauer, O. Brandt, L. Lee, and C. Ohm, ANUBIS: Proposal to search for long-lived neutral particles in CERN service shafts, arXiv:1909.13022.
[21] CMS Collaboration, Technical proposal for a mip timing detector in the cms experiment phase 2 upgrade, https://cds.cern.ch/record/2296612.
[22] C. Allaire *et al.*, Beam test measurements of low gain avalanche detector single pads and arrays for the ATLAS high granularity timing detector, J. Instrum. **13**, P06017 (2018).
[23] LHCb Collaboration, Expression of interest for a phase-II LHCb upgrade: Opportunities in flavour physics, and beyond, in the HL-LHC era, http://cds.cern.ch/record/2244311.
[24] LHCb Collaboration, The LHCb detector at the LHC, J. Instrum. **3**, S08005 (2008).
[25] D. Curtin and M. E. Peskin, Analysis of long lived particle decays with the MATHUSLA detector, Phys. Rev. D **97**, 015006 (2018).
[26] J. A. Evans, Detecting hidden particles with MATHUSLA, Phys. Rev. D **97**, 055046 (2018).
[27] J. L. Feng, I. Galon, F. Kling, and S. Trojanowski, Dark Higgs bosons at the forward search experiment, Phys. Rev. D **97**, 055034 (2018).

[28] F. Kling and S. Trojanowski, Heavy neutral leptons at FASER, Phys. Rev. D **97**, 095016 (2018).
[29] J. C. Helo, M. Hirsch, and Z. S. Wang, Heavy neutral fermions at the high-luminosity LHC, J. High Energy Phys. 07 (2018) 056.
[30] J. Liu, Z. Liu, and L.-T. Wang, Enhancing Long-Lived Particles Searches at the LHC with Precision Timing Information, Phys. Rev. Lett. **122**, 131801 (2019).
[31] J. L. Feng, I. Galon, F. Kling, and S. Trojanowski, Axion-like particles at FASER: The LHC as a photon beam dump, Phys. Rev. D **98**, 055021 (2018).
[32] O. Cerri, S. Xie, C. Pena, and M. Spiropulu, Identification of long-lived charged particles using time-of-flight systems at the upgraded LHC detectors, J. High Energy Phys. 04 (2019) 037.
[33] D. Curtin, K. R. Dienes, and B. Thomas, Dynamical dark matter, MATHUSLA, and the lifetime frontier, Phys. Rev. D **98**, 115005 (2018).
[34] A. Berlin and F. Kling, Inelastic dark matter at the LHC lifetime frontier: ATLAS, CMS, LHCb, CODEX-b, FASER, and MATHUSLA, Phys. Rev. D **99**, 015021 (2019).
[35] D. Dercks, J. De Vries, H. K. Dreiner, and Z. S. Wang, R-parity violation and light neutralinos at CODEX-b, FASER, and MATHUSLA, Phys. Rev. D **99**, 055039 (2019).
[36] D. Dercks, H. K. Dreiner, M. Hirsch, and Z. S. Wang, Long-lived fermions at AL3X, Phys. Rev. D **99**, 055020 (2019).
[37] F. F. Deppisch, W. Liu, and M. Mitra, Long-lived heavy neutrinos from Higgs decays, J. High Energy Phys. 08 (2018) 181.
[38] Z. Flowers, Q. Meier, C. Rogan, D. W. Kang, and S. C. Park, Timing information at HL-LHC: Complete determination of masses of Dark Matter and Long lived particle, J. High Energy Phys. 03 (2020) 132.
[39] J. H. Kim, S. D. Lane, H.-S. Lee, I. M. Lewis, and M. Sullivan, Searching for dark photons with maverick top partners, Phys. Rev. D **101**, 035041 (2020).
[40] J. D. Mason, Time-delayed electrons from Higgs decays to right-handed neutrinos, J. High Energy Phys. 07 (2019) 089.
[41] I. Boiarska, K. Bondarenko, A. Boyarsky, M. Ovchynnikov, O. Ruchayskiy, and A. Sokolenko, Light scalar production from Higgs bosons and FASER 2, J. High Energy Phys. 05 (2020) 049.
[42] J. M. No, P. Tunney, and B. Zaldivar, Probing dark matter freeze-in with long-lived particle signatures: MATHUSLA, HL-LHC and FCC-hh, J. High Energy Phys. 03 (2020) 022.
[43] A. Krovi, I. Low, and Y. Zhang, Higgs portal to dark QED, Phys. Rev. D **102**, 055003 (2020).
[44] K. Jodłowski, F. Kling, L. Roszkowski, and S. Trojanowski, Extending the reach of FASER, MATHUSLA, and SHiP towards smaller lifetimes using secondary particle production, Phys. Rev. D **101**, 095020 (2020).
[45] M. Du, Z. Liu, and V. Q. Tran, Enhanced long-lived dark photon signals at the LHC, J. High Energy Phys. 05 (2020) 055.
[46] F. Deppisch, S. Kulkarni, and W. Liu, Heavy neutrino production via Z' at the lifetime frontier, Phys. Rev. D **100**, 035005 (2019).
[47] M. Hirsch and Z. S. Wang, Heavy neutral leptons at ANUBIS, Phys. Rev. D **101**, 055034 (2020).
[48] C. Yuan, H. Zhang, Y. Zhao, and G. Chen, Producing and detecting long-lived particles at different experiments at the LHC, J. High Energy Phys. 02 (2022) 069.
[49] J. Liu, Z. Liu, L.-T. Wang, and X.-P. Wang, Enhancing sensitivities to long-lived particles with high granularity calorimeters at the LHC, J. High Energy Phys. 11 (2020) 066.
[50] H. K. Dreiner, J. Y. Günther, and Z. S. Wang, R-parity violation and light neutralinos at ANUBIS and MAPP, Phys. Rev. D **103**, 075013 (2021).
[51] J. De Vries, H. K. Dreiner, J. Y. Günther, Z. S. Wang, and G. Zhou, Long-lived sterile neutrinos at the LHC in effective field theory, J. High Energy Phys. 03 (2021) 148.
[52] E. Bertuzzo and M. Taoso, Probing light dark scalars with future experiments, J. High Energy Phys. 03 (2021) 272.
[53] F. Takahashi and W. Yin, Challenges for heavy QCD axion inflation, J. Cosmol. Astropart. Phys. 10 (2021) 057.
[54] G. Cottin, J. C. Helo, M. Hirsch, A. Titov, and Z. S. Wang, Heavy neutral leptons in effective field theory and the high-luminosity LHC, J. High Energy Phys. 09 (2021) 039.
[55] K. Cheung, K. Wang, and Z. S. Wang, Time-delayed electrons from neutral currents at the LHC, J. High Energy Phys. 09 (2021) 026.
[56] J. Guo, Y. He, J. Liu, and X.-P. Wang, Heavy long-lived coannihilation partner from inelastic dark matter model and its signatures at the LHC, arXiv:2111.01164.
[57] B. Bhattacherjee, S. Matsumoto, and R. Sengupta, Long-lived light mediators from Higgs boson decay at HL-LHC, FCC-hh and a proposal of dedicated LLP detectors for FCC-hh, arXiv:2111.02437.
[58] V. A. Mitsou, in *16th Marcel Grossmann Meeting on Recent Developments in Theoretical and Experimental General Relativity, Astrophysics and Relativistic Field Theories*, 2021, arXiv:2111.03036.
[59] A. Das, S. Goswami, K. N. Vishnudath, and T. K. Poddar, Freeze-in sterile neutrino dark matter in a class of U(1)′ models with inverse seesaw, arXiv:2104.13986.
[60] B. Holdom, Two U(1)'s and epsilon charge shifts, Phys. Lett. B **166**, 196 (1986).
[61] R. Foot and X.-G. He, Comment on Z Z-prime mixing in extended gauge theories, Phys. Lett. B **267**, 509 (1991).
[62] B. Kors and P. Nath, Aspects of the Stueckelberg extension, J. High Energy Phys. 07 (2005) 069.
[63] D. Feldman, Z. Liu, and P. Nath, Probing a Very Narrow Z-Prime Boson with CDF and D0 Data, Phys. Rev. Lett. **97**, 021801 (2006).
[64] D. Feldman, Z. Liu, and P. Nath, The stueckelberg Z prime at the LHC: Discovery potential, signature spaces and model discrimination, J. High Energy Phys. 11 (2006) 007.
[65] D. Feldman, Z. Liu, and P. Nath, The stueckelberg Z-prime extension with kinetic mixing and milli-charged dark matter from the hidden sector, Phys. Rev. D **75**, 115001 (2007).

[66] D. Feldman, Z. Liu, P. Nath, and B. D. Nelson, Explaining PAMELA and WMAP data through coannihilations in extended SUGRA with collider implications, Phys. Rev. D **80**, 075001 (2009).
[67] M. Buschmann, J. Kopp, J. Liu, and P. A. N. Machado, Lepton jets from radiating dark matter, J. High Energy Phys. 07 (2015) 045.
[68] C. A. Argüelles, X.-G. He, G. Ovanesyan, T. Peng, and M. J. Ramsey-Musolf, Dark gauge bosons: LHC signatures of non-abelian kinetic mixing, Phys. Lett. B **770**, 101 (2017).
[69] S. Davidson, S. Hannestad, and G. Raffelt, Updated bounds on millicharged particles, J. High Energy Phys. 05 (2000) 003.
[70] ArgoNeuT Collaboration, Improved Limits on Millicharged Particles Using the ArgoNeuT Experiment at Fermilab, Phys. Rev. Lett. **124**, 131801 (2020).
[71] A. Ball *et al.*, Search for millicharged particles in proton-proton collisions at $\sqrt{s} = 13$ TeV, Phys. Rev. D **102**, 032002 (2020).
[72] ALEPH, DELPHI, L3, OPAL, SLD, LEP Electroweak Working Group, SLD Electroweak Group, SLD Heavy Flavour Group Collaborations, Precision electroweak measurements on the Z resonance, Phys. Rep. **427**, 257 (2006).
[73] ATLAS Collaboration, Search for high-mass dilepton resonances using 139 fb^{-1} of pp collision data collected at $\sqrt{s} = 13$ TeV with the ATLAS detector, Report No. ATLAS-CONF-2019-001, 2019.
[74] ATLAS Collaboration, Search for dark matter and other new phenomena in events with an energetic jet and large missing transverse momentum using the ATLAS detector, J. High Energy Phys. 01 (2018) 126.
[75] K. K. Boddy, V. Gluscevic, V. Poulin, E. D. Kovetz, M. Kamionkowski, and R. Barkana, Critical assessment of CMB limits on dark matter-baryon scattering: New treatment of the relative bulk velocity, Phys. Rev. D **98**, 123506 (2018).
[76] R. de Putter, O. Doré, J. Gleyzes, D. Green, and J. Meyers, Dark Matter Interactions, Helium, and the Cosmic Microwave Background, Phys. Rev. Lett. **122**, 041301 (2019).
[77] E. D. Kovetz, V. Poulin, V. Gluscevic, K. K. Boddy, R. Barkana, and M. Kamionkowski, Tighter limits on dark matter explanations of the anomalous EDGES 21 cm signal, Phys. Rev. D **98**, 103529 (2018).
[78] LHC long term schedule, https://lhc-commissioning.web.cern.ch/schedule/LHC-long-term.htm.
[79] FASER Collaboration, Detecting and studying high-energy collider neutrinos with FASER at the LHC, Eur. Phys. J. C **80**, 61 (2020).
[80] B. Isildak, FACET: Forward-apertrue cms extension, https://indico.cern.ch/event/980853/contributions/4361208/attachments/2251302/3819062/FACET_LLP9.pdf.
[81] M. Albrow *et al.*, A Long-Lived Particle and Dark Matter Search at the LHC at $z = 80$–127 m, https://www.snowmass21.org/docs/files/summaries/EF/SNOWMASS21-EF9_EF8_ALBROW-111. pdf.
[82] M. Albrow (private communication).
[83] ATLAS LAr-HGTD Group Collaboration, A high-granularity timing detector in ATLAS: Performance at the HL-LHC, Nucl. Instrum. Methods Phys. Res., Sect. A **924**, 355 (2019).
[84] L. C. García, A high-granularity timing detector for the phase-II upgrade of the ATLAS calorimeter system: Detector concept, description, R&D and beam test results, J. Instrum. **15**, C09047 (2020).
[85] Z. Flowers, Q. Meier, C. Rogan, D. W. Kang, and S. C. Park, Timing information at HL-LHC: Complete determination of masses of Dark Matter and Long lived particle, J. High Energy Phys. 03 (2020) 132.
[86] B. Bhattacherjee, S. Mukherjee, R. Sengupta, and P. Solanki, Triggering long-lived particles in HL-LHC and the challenges in the rst stage of the trigger system, J. High Energy Phys. 08 (2020) 141.
[87] R. E. Shrock, A Test for the Existence of Effectively Stable Neutral Heavy Leptons, Phys. Rev. Lett. **40**, 1688 (1978).
[88] FMMF Collaboration, Search for neutral weakly interacting massive particles in the Fermilab Tevatron wide band neutrino beam, Phys. Rev. D **52**, 6 (1995).
[89] B. Batell, M. Pospelov, and A. Ritz, Exploring portals to a hidden sector through fixed targets, Phys. Rev. D **80**, 095024 (2009).
[90] Particle Data Group, Review of particle physics, Prog. Theor. Exp. Phys. **2020**, 083C01 (2020).
[91] T. Pierog, Iu. Karpenko, J. M. Katzy, E. Yatsenko, K. Werner, EPOS LHC: Test of collective hadronization with data measured at the CERN Large Hadron Collider, Phys. Rev. C **92**, 034906 (2015).
[92] R. U. C. Baus and T. Pierog, Cosmic ray Monte Carlo (CRMC), https://web.ikp.kit.edu/rulrich/crmc.html.
[93] T. Sjöstrand, S. Ask, J. R. Christiansen, R. Corke, N. Desai, P. Ilten, S. Mrenna, S. Prestel, C. O. Rasmussen, and P. Z. Skands, An introduction to PYTHIA 8.2, Comput. Phys. Commun. **191**, 159 (2015).
[94] E. Fermi, On the theory of the impact between atoms and electrically charged particles, Z. Phys. **29**, 315 (1924).
[95] E. J. Williams, Nature of the high-energy particles of penetrating radiation and status of ionization and radiation formulae, Phys. Rev. **45**, 729 (1934).
[96] C. F. von Weizsacker, Radiation emitted in collisions of very fast electrons, Z. Phys. **88**, 612 (1934).
[97] Particle Data Group, Review of particle physics, Phys. Rev. D **98**, 030001 (2018).
[98] J. Blümlein and J. Brunner, New exclusion limits on dark gauge forces from proton bremsstrahlung in beam-dump data, Phys. Lett. B **731**, 320 (2014).
[99] K. J. Kim and Y.-S. Tsai, Improved weizsacker-williams method and its application to lepton and W boson pair production, Phys. Rev. D **8**, 3109 (1973).
[100] Y.-S. Tsai, Pair production and bremsstrahlung of charged leptons, Rev. Mod. Phys. **46** (1974) 815; **49**, 421(E) (1977).
[101] A. Faessler, M. I. Krivoruchenko, and B. V. Martemyanov, Once more on electromagnetic form factors of nucleons in extended vector meson dominance model, Phys. Rev. C **82**, 038201 (2010).
[102] A. Alloul, N. D. Christensen, C. Degrande, C. Duhr, and B. Fuks, FeynRules 2.0—A complete toolbox for tree-level phenomenology, Comput. Phys. Commun. **185**, 2250 (2014).

[103] J. Alwall, R. Frederix, S. Frixione, V. Hirschi, F. Maltoni, O. Mattelaer, H.-S. Shao, T. Stelzer, P. Torrielli, and M. Zaro, The automated computation of tree-level and next-to-leading order differential cross sections, and their matching to parton shower simulations, J. High Energy Phys. 07 (2014) 079.
[104] L. Carloni and T. Sjostrand, Visible effects of invisible hidden valley radiation, J. High Energy Phys. 09 (2010) 105.
[105] L. Carloni, J. Rathsman, and T. Sjostrand, Discerning secluded sector gauge structures, J. High Energy Phys. 04 (2011) 091.
[106] Y. Bai and Z. Han, Measuring the Dark Force at the LHC, Phys. Rev. Lett. **103**, 051801 (2009).
[107] M. Kim, H.-S. Lee, M. Park, and M. Zhang, Examining the origin of dark matter mass at colliders, Phys. Rev. D **98**, 055027 (2018).
[108] J. Chen, P. Ko, H.-N. Li, J. Li, and H. Yokoya, Light dark matter showering under broken dark $U(1)$—revisited, J. High Energy Phys. 01 (2019) 141.
[109] R. D. Ball *et al.*, Parton distributions with LHC data, Nucl. Phys. **B867**, 244 (2013).
[110] R. D. Ball *et al.*, The path to proton structure at one-percent accuracy, arXiv:2109.02653.
[111] T.-J. Hou *et al.*, Progress in the CTEQ-TEA NNLO global QCD analysis, arXiv:1908.11394.
[112] LHCb Collaboration, Search for $A' \to \mu^+\mu^-$ Decays, Phys. Rev. Lett. **124**, 041801 (2020).
[113] J. Blumlein and J. Brunner, New exclusion limits for dark gauge forces from beam-dump data, Phys. Lett. B **701**, 155 (2011).
[114] J. Blümlein and J. Brunner, New exclusion limits on dark gauge forces from proton bremsstrahlung in beam-dump data, Phys. Lett. B **731**, 320 (2014).
[115] S. N. Gninenko, Constraints on sub-GeV hidden sector gauge bosons from a search for heavy neutrino decays, Phys. Lett. B **713**, 244 (2012).
[116] J. D. Bjorken, S. Ecklund, W. R. Nelson, A. Abashian, C. Church, B. Lu, L. W. Mo, T. A. Nunamaker, and P. Rassmann, Search for neutral metastable penetrating particles produced in the SLAC beam dump, Phys. Rev. D **38**, 3375 (1988).
[117] Darkcast, https://gitlab.com/philten/darkcast.
[118] LSND Collaboration, Evidence for $\nu_\mu \to \nu_e$ oscillations from pion decay in flight neutrinos, Phys. Rev. C **58**, 2489 (1998).
[119] J. H. Chang, R. Essig, and S. D. McDermott, Revisiting supernova 1987A constraints on dark photons, J. High Energy Phys. 01 (2017) 107.
[120] LHCb Collaboration, Searches for low-mass dimuon resonances, J. High Energy Phys. 10 (2020) 156.
[121] D. Green, Status of FACET (Forward-aperture CMS extension), https://indico.cern.ch/event/1042226/contributions/4600237/attachments/2342545/3993943/Status%20of%20-FACET_11_2021_v4. ppt.